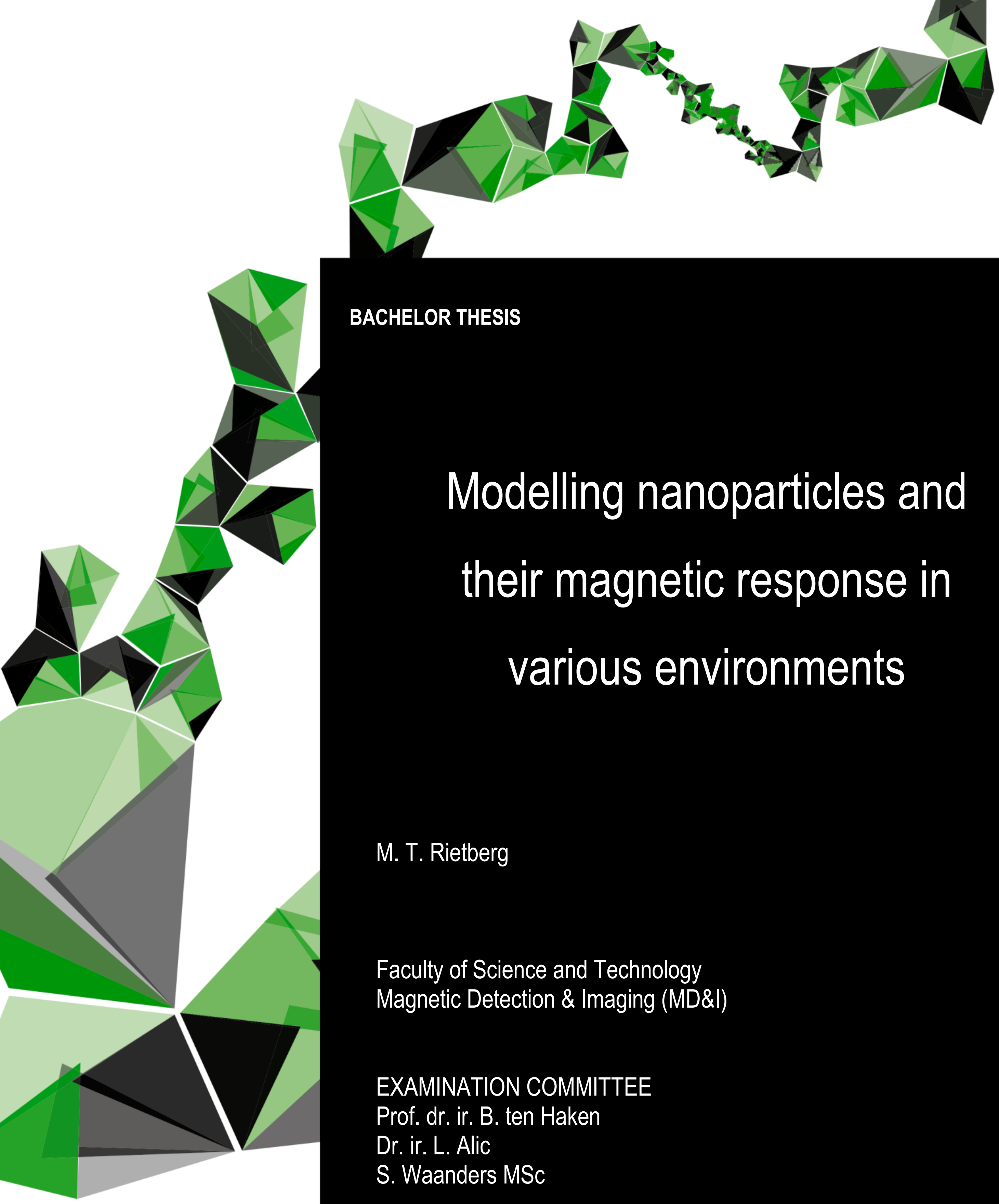

BACHELOR THESIS

Modelling nanoparticles and their magnetic response in various environments

M. T. Rietberg

Faculty of Science and Technology
Magnetic Detection & Imaging (MD&I)

EXAMINATION COMMITTEE
Prof. dr. ir. B. ten Haken
Dr. ir. L. Alic
S. Waanders MSc

2020-06-29

UNIVERSITY OF TWENTE.

Abstract

In this study, the magnetic behaviour of superparamagnetic nanoparticles in various environments is modelled, which have their clinical significance in e.g. the sentinel node biopsy. This was done using the Legendre expansion of two Fokker-Plank equations, one for Brownian and one for Néel relaxation. The voltage as measured with SPaQ can be approximated with the combined result of these. Based on verification with experimental data, it can be said that this model accurately reflects the behavior of the tested particles, with the exception of a flower-shaped particle.

Contents

Chapter 1

Introduction

Superparamagnetic iron-oxide nanoparticles are currently used experimentally in biomedical applications as a tracer in novel magnetic detection & imaging techniques, e.g. drug delivery, magnetic particle spectroscopy (MPS), magnetic particle imaging (MPI), magnetic resonance imaging (MRI), magnetic fluid hyperthermia, and sentinel lymph node biopsy (SLNB). SLNB is a surgical protocol to personalize cancer treatment that establishes if the tumour has metastasized trough finding, removing and then analysing the sentinel nodes [1]. Traditionally, a radioactive tracer used for SLNB has drawbacks such as a limited availability, a short shelf life and infrastructural problems [2]. Magnetic nanoparticles do not have these drawbacks, instead they are more beneficial for patient and physicians.

Figure 1.1: The Sentimag® probe

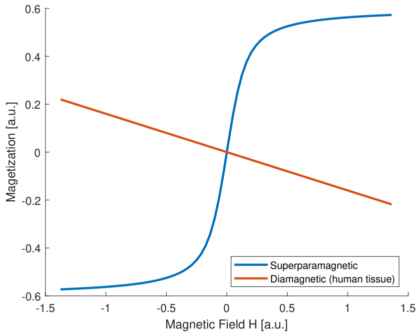

Figure 1.2: Magnetic response, based on [3], not to scale.

A medical device for detection of nanoparticles in clinical setting is currently available in the form of the Sentimag® magnetic probe (Endomag, seen in Figure 1.1). This probe is however, not only sensitive to the nanoparticles, but also the human body, since it uses linear detection, which can limit its performance [4].

In magnetic SLNB, superparamagnetic particles are injected in or near the tumour and drained trough the lymphatic system to the near lymph nodes (LN) where they will accumulate [5]. The LN near to the primary tumour is (functionally) labeled the sentinel node, and can be detected by a magnetic probe due to accumulation of the nanoparticles. Research has shown that the performance of these tracers is comparable to the radioactive tracers [6] and that the magnetic SNLB procedure can be performed easily and safely [7]. However, even though there is a vivid field developing new nanoparticles, the clinical applications are limited by sheer number of specialized nanoparticles available for clinical use. Further development would greatly be supported by better understanding of the behaviour of nanoparticles in a biological environment. Therefore, the aim of this undergraduate work is as follows:

Modelling the magnetic behaviour of superparamagnetic nanoparticles in various environments

Various models are available for characterization of nanoparticles and their response to applied magnetic field, e.g. effective relaxation time [8] and the Langevin [9]. However, these models do not predict the nanoparticle behaviour accurately, especially in the case were the two relaxation mechanisms (Brownian and Néel) both play a significant role. A better approach of modelling the particles should result in an accurate validation and prediction of nanoparticle behaviour. Furthermore, this approach is also useful for designing nanoparticles for a specific goal (e.g. imaging, cancer therapy, hyperthermia and targeted drug or gene delivery). The models developed as a part of this work are validated with four nanoparticle (Resovist, Sienna, Magtrace, Synomag) in multiple environments (viscosity and particle densities). The experimental data used for the validation is acquired trough a LangevinSweep using the superparamagnetic quantifier (SPaQ) [10].

Chapter 2

Theory

Magnetic materials, regardless the applications, can categorized trough their magnetic behaviour (M) in response to an applied magnetic field (AMF) (B). The magnetic flux density (B, [T]) of the AMF can be expressed through the magnetic field vector (H, [A/m]) and the magnetization vector (M, [A/m]) [11]:

$$B = \mu H = \mu_0(1 + \chi)H = \mu_0(H + M) \tag{2.1}$$

with μ the magnetic permeability of the material [N/A^2], μ_0 magnetic permeability of a vacuum ($4\pi \cdot 10^{-7}$ N/A^2), and χ the magnetic susceptibility [dimensionless]. The magnetic susceptibility measures the ratio of magnetized material in an AMF, an intrinsic property of the material and is here to be assumed steady-state. The magnetization vector indicates the magnetic dipole moment per volume and represents the interaction of the applied field on the material [12]. This response is material dependent, and as such categorizes magnetic materials on their response in certain categories: ferro-, dia-, para- and superparamagnetic [13]. Figure 2.1 illustrates the magnetic behaviour van these materials. Only ferromagnetic materials have the property to hold their magnetization (well) after removal of the applied field, which makes it possible to create permanent magnets out of ferromagnets. It can also be observed that diamagnetic and paramagnetic materials respond linearly to changes in the applied field, this means their magnetic susceptibility stays constant for any AMF. Additionally, the susceptibility of ferromagnetic and superparamagnetic materials dependent strongly on the applied field [13]. For superparamagnetic materials, the steepness at zero field originates in its sufficiently small particle size, the magnetic energy is smaller than the thermal fluctuations [14]. Since human tissue is slightly diamagnetic (and therefore exhibits a linear response to an AMF), the materials with non-linear magnetic response can easily be detected inside human tissue [15]. This is what is used in the SPaQ (SuperParamagnetic Quantifier) magnetometer.

The susceptibility of materials in a time-varying magnetic field actually also dependents on the frequency of this very field [16]. With the frequency at a certain level, particles will not have enough time to keep up and lag behind due to the finite nature of their relaxation times. Consequently, the magnetization follows the exponentially decay in frequency with relaxation time τ_{eff} [s] and the magnetic susceptibility follows Debye's relaxation law [17], [18]:

$$\chi(\omega) = \chi_0 \frac{1}{1 + i\omega\tau_{\text{eff}}} \tag{2.2}$$

with ω the angular frequency of the AMF and χ_0 the static susceptibility.

This relaxation time, τ_{eff}, is the result of two separate relaxation mechanisms: Brownian en Néel [16]. The key difference between these two is that Brownian relaxation describes the rotation of the particle itself and Néel relaxation describes the rotation of the magnetic moment inside the particle [16], as can be seen in Figure 2.2.

The change in the magnetization for pure Brownian motion is due the rotation of the particle while the internal magnetization remains fixed regarding the crystalline lattice. Brownian relaxation is described by [12]:

$$\tau_{\text{B}} = \frac{3\eta V_h}{k_B T} \tag{2.3}$$

Here it is shown that Brownian relaxation is dependent of multiple parameters including the medium viscosity (η, [Pa s]), the hydrodynamic volume of the (monodisperse) particle (V_h, [m^3]) and the temperature (T, [K]). Here k_B is Boltzmann's constant ($1.38064852 \cdot 10^{-23}$ J/K).

A pure Néel relaxation changes the magnetization due to rotation of the internal magnetization with respect to the crystalline lattice, while the particle itself does not rotate [16]. In literature Néel relaxation is described with different equations, one often used is the Néel-Arrhenius equation [12]:

$$\tau_N = \tau_0 \; exp(\frac{KV_c}{k_B T}) \tag{2.4}$$

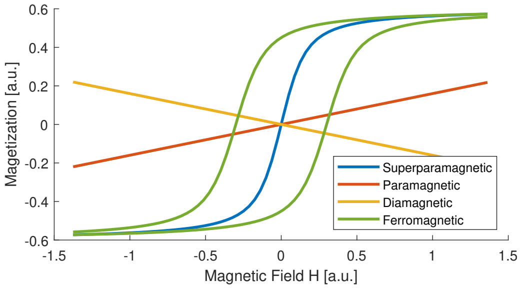

Figure 2.1: Magnetic response of different types of magnetic materials (ferro-, dia-, para- and superparamagnetic) to the AMF. Magnetization curve is not to scale, based on [3]

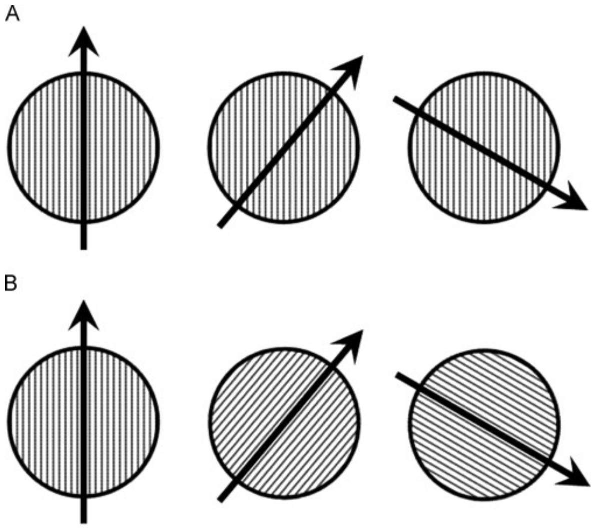

Figure 2.2: The two different relaxation mechanisms for superparamagnetic materials, A: Néel and B: Brownian [19].

The parameters in this equation are: the attempt time or attempt period (τ_0, typical values between 10^{-9} and 10^{-10}s [20], the average time between two successive random thermal excitations), anisotropy energy (K, [J/m^3]) and the core volume of the (monodisperse) particle (V_c, [m^3]) [21].
A more descriptive one sounds as following [22]:

$$\tau_N = \frac{\sqrt{\pi}\beta(1+\alpha'^2)M_s}{4\gamma\alpha'(\beta K)^{3/2}}e^{\beta K} \tag{2.5}$$

with $\beta = V_c/(k_B T)$. This equation also has the following parameters: the saturation magnetization (M_s, [A/m]) and damping constant (α', [-]). γ is the electron gyromagnetic ratio ($1.76 \cdot 10^{11}$ rad/s T).
While it is easy to assume that particles responds with pure Brownian or pure Néel relaxation, this may often not be the case. The following equation accounts for both relaxation mechanisms simultaneously [20], [23]:

$$\tau_{\text{eff}} = \frac{\tau_B \tau_N}{\tau_B + \tau_N} \tag{2.6}$$

The parameters of this equation are defined in equations 2.3 and 2.5, the equation is graphically shown in Figure 2.3. Here it is assumed that both relaxation mechanisms are not dependent on the magnetic field, and do not influence each other.
The effective relaxation time can be substituted to equation 2.2 to calculate the magnetic susceptibility of the material. However, this approach does not always hold due to the underlying assumptions:

- Assumption that relaxation happens the same regardless of field strength. This is incorrect, these mechanisms, in particular Néel relaxation, are dependent on the field strength [23].

- Assumption that the particles are monodisperse, which does not reflect the real world accurately [25]

- Assumption that Brownian and Néel relaxation are decoupled and do not influence each other, which is however not what is expected [23].

- Assumption that a changing magnetic field has no effect. Even with magnetic field taken into account when calculating relaxation times, a continuously changing magnetic field introduces other behaviour changes [23]. An example is phase delays, these behaviour changes need to be incorporated into the model, which Equation 2.6 cannot do.

Therefore, another approach is necessary, one which reflects the behaviour of combined Brownian and Néel relaxation more closely.

An better approach starts with considering an ensemble of spherical particles in a ferrofluid. In this ensemble, each particle is described by a constant magnetic dipole moment $\overrightarrow{m_0}$ with the magnitude of $m_0 = M_s V_c$ [23]. The distribution of these moments in the ensemble is given as $W(x,t)$ where the applied field defines $\overrightarrow{B}(t) = B(t)\hat{z}$. Moreover, θ is the polar angle between $\overrightarrow{m_0}$ and $\hat{z}$, which concludes in $x \equiv cos(\theta)$. An additional assumption is that there are two relaxation mechanisms, namely the Brownian and Néel relaxation. These mechanisms are both responsible for aligning the magnetic dipole moment with the applied field, but due to thermal interactions with the surrounding environment there will a randomization of the orientation and the alignment will not be completed [23]. To simplify the calculations two equations are considered where either Brownian or Néel relaxation is dominant.
Beginning with the equation for Brownian relaxation. Here the magnetic dipole moment is free to rotate trough rotation of the particle as a whole. This Fokker-Planck partial differential equation describes the evolution of $W(x,t)$ over time [17], [23], [22]:

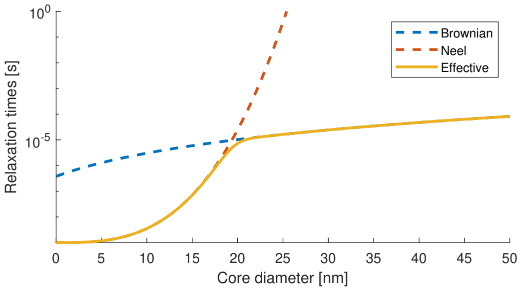

Figure 2.3: Relaxation times against core diameter, based on [24]. Here it can be seen that there is a region where Néel and a region where Brownian relaxation are dominant, but also a region where they both play a role.

$$\frac{\partial W}{\partial t} = \frac{\partial}{\partial x}\left[(1-x^2)\left(\frac{\partial W}{\partial x} - \alpha(t)W\right)\right]\frac{1}{2\tau_{B0}} \tag{2.7}$$

Here $\tau_{B0} \equiv \frac{3\eta V_h}{k_B T}$ and $\alpha(t) \equiv \frac{m_0}{k_B T}B(t)$.

The other equation is for Néel relaxation, where the magnetic dipole moment can freely rotate relative to the crystalline lattice. Here it is assumed that the particles cannot rotate, the magnetic interaction energy is axisymmetric (has rotational symmetry with respect to the axis) and that for every particle the the easy axis (the dipole will align with this axis when there is no applied field and the magnetic interaction energy is minimal) is aligned along the z-axis. This results in the following Fokker-Planck partial differential equation for the evolution of $W(x,t)$ over time [17], [23], [22]:

$$\frac{\partial W}{\partial t} = \frac{\partial}{\partial x}\left[(1-x^2)\left(\frac{\partial W}{\partial x} - \alpha(t)W - \alpha_K x W\right)\right]\frac{1}{2\tau_{N0}} \tag{2.8}$$

Here $\tau_{N0} \equiv \frac{\beta(1+\alpha'^2)M_s}{2\gamma\alpha'}$ and $\alpha_K = 2K\beta$. However, sometimes Brownian relaxation is prohibited, which happens in high-viscosity environments and when the particles are fixed. This means that the easy axis will keep its random rotation since it will not be able to rotate freely. For these cases it is useful to replace K with an effective anisotropy energy according to $K_{\text{eff}} = \frac{1}{3}K$.

From these equations one needs to find $W(x,t)$ (which needs to be normalized according to $\int_{-1}^{1} W(x,t)dx = 1$) to get $\langle x(t)\rangle$, according to [23]:

$$\langle x(t)\rangle = \int_{-1}^{1} xW(x,t)dx \tag{2.9}$$

After this it is possible to calculate the magnetization of the ensemble:

$$\overrightarrow{M}(t) = nm_0\langle x(t)\rangle\hat{z} \tag{2.10}$$

Here n is the nanoparticle number density [m^3]. Since there are two Fokker-Planck equations, the resulting magnetization equations need to combined in a latter stadium However, the equations which need to be solved for this (2.7 and 2.8) have no known analytical solution. This is why solutions are often approximated numerically through Legendre polynomials, as was done in this thesis.

Instead of solving equation 2.7 numerically it is also possible to approach this adiabatically, which involves more assumptions. Adiabatic conditions imply that there is a continuous equilibrium; the applied field and the distribution of magnetic moments stays constant in time. If one ignores the equilibrium condition and assume that the particles find equilibrium immediately in the changing applied field, the solution will be the Langevin equation [17]:

$$M(t) = M_s\mathcal{L}(\alpha) \text{ where } \mathcal{L}(\alpha) = coth(\alpha) - \alpha^{-1} \tag{2.11}$$

Here α is the same as in equation 2.7, namely $\alpha(t) \equiv \frac{m_0}{k_B T} B(t)$. Due to the underlying assumptions, this equation does not describe the magnetization curve of superparamagnetic particles in detail well. Surface coating [26], anisotropic effects [27] and strong interactions [28] makes the Langevin equation even less precise. Since this equation is, however, often used, it shall be used to compare against the approach mentioned before.

Chapter 3

Methods

3.1 Model

As mentioned before, the Fokker-Planck equations for Brownian and Néel relaxation (2.7 and 2.8) have no known analytical solution, and needs a numerical approximation. Legendre expansion provides a solution for this approximation [22] by expansion of $W(x,t)$ in terms of Legendre polynomials and substitution to 2.7 and 2.8.:

$$W(x,t) = \sum_{n=0}^{\infty} a_n(t) P_n(x) \tag{3.1}$$

When substituting equation 3.1 in 2.7 it leads, using standard recursion and orthogonality for Legendre polynomials, to the following ordinary differential equation [23]:

$$\frac{2\tau_{B0}}{n(n+1)} \frac{da_n}{dt} = -a_n + \alpha(t) \left[\frac{a_{n-1}}{2n-1} - \frac{a_{n+1}}{2n+3} \right] \tag{3.2}$$

There are two things to note about this function, namely that the normalization condition determines that $a_0(t) = 0.5$ and that $\langle x(t) \rangle = (2/3)a_1(t)$.
This equation can also be rewritten in the form of a matrix equation, by truncating after N terms:

$$\tau_0 \frac{d\mathbf{y}}{dt} = \mathbf{A}\mathbf{y} + \mathbf{b} \tag{3.3}$$

Here $\mathbf{A}$ is a N by N matrix, $\mathbf{y}$ and $\mathbf{b}$ are both column vectors of N elements. $\mathbf{y}$ contains the elements $a_1, a_2, ..., a_N$. A matrix equation is often (not always) easier for computers to calculate with, which is important for intensive numerical integration of ordinary differential equations.
For Brownian relaxation one fills in: $\tau_0 = \tau_{B0}$ and $\mathbf{b}_1 = \alpha/2$, the rest of $\mathbf{b}$ is zero. $\mathbf{A}$

will become a tridiagonal matrix with [23]:

$$\begin{aligned}
A_{n,n} &= -\frac{n(n+1)}{2} \text{ for } n = 1, 2, ..., N \\
A_{n,n+1} &= -\frac{n(n+1)}{2(2n+3)}\alpha \text{ for } n = 1, 2, ..., N-1 \\
A_{n,n-1} &= \frac{n(n+1)}{2(2n-1)}\alpha \text{ for } n = 2, 3, ..., N
\end{aligned} \tag{3.4}$$

The remaining components of **A** will be zero.
For Néel relaxation, one can follow the same path, by substituting equation 3.1 in 2.8. This leads to the following ordinary differential equation [23]:

$$\begin{aligned}
\frac{2\tau_{N0}}{n(n+1)}\frac{da_n}{dt} =& -a_n + \alpha(t)\left[\frac{a_{n-1}}{2n-1} - \frac{a_{n+1}}{2n+3}\right] + \alpha_K\left[\frac{(n-1)a_{n-2}}{(2n-3)(2n-1)}\right. \\
&\left. + \frac{na_n}{(2n-1)(2n+1)} - \frac{(n+1)a_n}{(2n+1)(2n+3)} - \frac{(n+2)a_{n+2}}{(2n+3)(2n+5)}\right]
\end{aligned} \tag{3.5}$$

Again, because of the normalization condition, $a_0(t) = 0.5$ and also $\langle x(t)\rangle = (2/3)a_1(t)$. This equation can as well be rewritten in the form of a matrix equation, by truncating after N terms according to 3.3. For Néel relaxation one fills in: $\tau_0 = \tau_{N0}$ and $\mathbf{b}_1 = \alpha/2$, $\mathbf{b}_2 = \alpha_K/2$, the rest of $\mathbf{b}$ is zero. **A** will become a pentadiagonal matrix with [23]:

$$\begin{aligned}
A_{n,n} &= \frac{n(n+1)}{2}\left[-1 + \frac{n\alpha_K}{(2n-1)(2n+1)} - \frac{(n+1)\alpha_K}{(2n+1)(2n+3)}\right] \text{ for } n = 1, 2, ..., N \\
A_{n,n+1} &= -\frac{n(n+1)}{2(2n+3)}\alpha \text{ for } n = 1, 2, ..., N-1 \\
A_{n,n-1} &= \frac{n(n+1)}{2(2n-1)}\alpha \text{ for } n = 2, 3, ..., N \\
A_{n,n+2} &= -\frac{n(n+1)(n+2)}{2(2n+3)(2n+5)}\alpha_K \text{ for } n = 1, 2, ..., N-2 \\
A_{n,n-2} &= \frac{n(n+1)(n-1)}{2(2n-3)(2n-1)}\alpha_K \text{ for } n = 3, 4, ..., N
\end{aligned} \tag{3.6}$$

Again, the remaining components of **A** will be zero.
After evaluation of the Fokker-Planck equations for both relaxation mechanisms trough Legendre expansion, one can extract $\langle x(t)\rangle$ and calculate the time derivative of the magnetization:

$$\frac{d}{dt}M(t) = nM_sV_c\frac{d}{dt}\langle x(t)\rangle \tag{3.7}$$

This needs to be done for both Brownian and Néel, the resulting magnetization responses can be combined using:

$$\frac{d}{dt}M(t) = \sqrt{\left(\frac{d}{dt}M_{Brownian}(t)\right)^2 + \left(\frac{d}{dt}M_{Néel}(t)\right)^2} \tag{3.8}$$

To compare this against the Langevin function, here one finds the peak magnetic response by:

$$\left[\frac{d}{dt}M(t)\right]_{peak} = nM_sV_cf\left[\mathcal{L}(\alpha_+) - \mathcal{L}(\alpha_-)\right] \tag{3.9}$$

Where $\alpha_\pm$ is the field parameters given by $\frac{V_cM_s}{k_BT}(B_{DC} \pm B_{AC})$, when the magnetic field is given by equation 3.12.

Up until now, it was assumed there was a monodisperse mixture, all particles are the same size. However, this is not true, practically an ensemble of nanoparticles is often polydisperse [29]. The magnetic susceptibility of these different sizes can be considered additive, but since each particle size will not be present with the same frequency, a weight must be allocated. This weight $D(d_c)$ is calculated according to:

$$\frac{d}{dt}M(t) = nM_s \lim_{n\to\infty}\sum_{i=1}^{n} D(\frac{d_{c,i}+d_{c,i-1}}{2})\Delta d_c V_c \frac{d}{dt}\langle x_i(t)\rangle \tag{3.10}$$

Where $d_{c,i} = i \cdot \Delta d_c$ and $\Delta d_c = upperlim/n$. $\langle x_i(t)\rangle$ indicates the calculated expectation value for $x(t)$ for the respective $\frac{d_{c,i}+d_{c,i-1}}{2}$. For these calculations, one also needs to take into account that every core diameter corresponds to a different hydrodynamic diameter and anisotropy constant. Since infinity is quite computational extensive, a approximation can be made by taking the limit to a finite number. This means to solve a series of the ordinary differential equations for a finite number of size bins and sum the result, while taking into account the weight of each bin.

The characteristics of the nanoparticle can be captured trough the Particle Response Function (PRF), which can be obtained by simulating the nanoparticles with:

$$B(t) = B_{AC}\ sin(2\pi ft) + \dot{B}_+\ t \tag{3.11}$$

The PRF, seen in Figure 3.1 is the time derivative of the calculated magnetization curve $\partial M/\partial H$ [31]. This means that, given the fact that $M = 0$ for $\mu_0 H = 0$, integration of the PRF gives a magnetization curve as shown in figure 2.1. One might argue that the received function could show the non-linearity of the particle even better. This function is similar to the Point Spread Function in x-space for MPI, it has even other more names in literature. However, it was decided to refer to this function as PRF, since it is an elegant and clear description; the function describes the measured response of the particles.

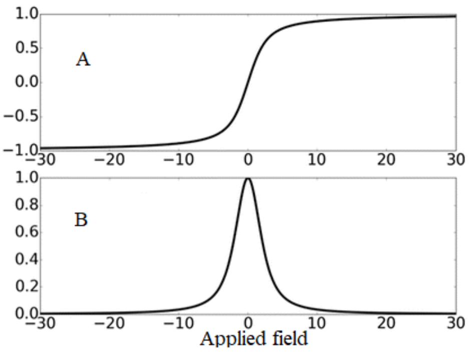

Figure 3.1: A: Magnetization curve and B: PRF [30]

3.2 Model verification

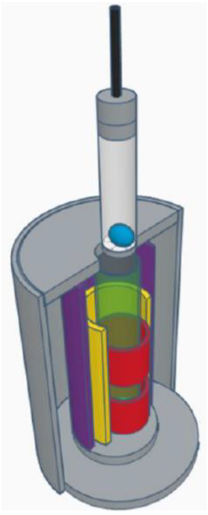

Figure 3.2: The SPaQ setup from [32]

To verify this model, one can use a Langevin sweep of the SuperParamagnetic Quantifier (SPaQ), the setup can be seen in Figure 3.2. SPaQ exploits the non-linear response of the superparamagnetic particles to external magnetic fields, which differs from the linear response of human tissue [33]. The technique uses a combined alternating (AC) and constant (DC) magnetic field, according to:

$$B(t) = B_{AC}\ sin(2\pi f t) + B_{DC} \tag{3.12}$$

which looks quite the same as Equation 3.11. The SPaQ approach makes it possible to detect particles in the measurement due to their unique response to the applied magnetic field. However, the measurements show magnetization with an incoming coil voltage (U_{det}, [V]), it is therefore useful to connect the actual magnetization to this coil voltage. For this, one can use the following equation [15]:

$$U_{det}(t)/S_{coil} = -\frac{d}{dt}M(t) \tag{3.13}$$

Here S_{coil} is the coil sensitivity, for the SPaQ magnetometer this value is 37.8 mT/A. The model as whole was developed using MATLAB® ver. 2020a and validated with four different particles, namely Resovist®, Sienna®, Magtrace® and Synomag®, in certain environments. To review the behaviour of these particles the model takes in the following parameters:

- Temperature [K]
- Viscosity [Pa s]
- Particle number density [m^3]
- Alternating magnetic field strength [T]
- Coil constant [T/A]
- Particle size distribution [nm]
- Hydrodynamic shell size [nm]
- Saturation magnetization [J m^{-3} T^{-1}]
- Anisotropy constant distribution [J m^{-3}]

The output of the model consists of a magnetization curve and its corresponding PRF. In addition to this, the PRF is quantified on its Full Width Half Maximum (FWHM) and maximum value ($dH/dM_{\max}$). To review its behaviour, a verification is nesisarry. After establishing a baseline with Resovist® in water, the model will be verified with

Resovist® in glycerol. This fluid has a higher viscosity, which shows if the model can handle a different for this parameter. In the next experiment there will be a difference in particle, namely the model will be verified with Sienna®, Magtrace® and Synomag® instead of Resovist®. It is interesting to note that Synomag® is very different from the other particles because of its morphology. Namely, Synomag® consist of a cluster of smaller particles in the form of a flower. Finally, the model will be verified with Magtrace® in different densities; for 40 µg/µL, 80 µg/µL and 120 µg/µL in demiwater. For every measurement there will be a gain of 1000, which will be removed afterwards. Moreover, where possible, the measurements will be repeated and their results averaged.

Chapter 4

Results

4.1 Model

Before introducing experimental data, it is interesting to review the model to analyse its behaviour. Resovist® was used as baseline, and when the model was run, one by one most of the input parameters were first halved and then doubled. After this, the result of those changes was plotted against the baseline, as can be seen in figure 4.1. The quantification of each of those PRFs is noted in table 4.1.

For a lot of the parameters, a change in magnitude means that the PRF changes with more or less the same factor (linearly correlated), which means that the figures look quite the same. These parameters are: the coil constant, the particle number density, the alternating magnetic field density and its frequency. This statements holds the strongest for the former two, namely since the FWHM does not change with a change in those parameters. Next, there are two sets each of two parameters which behaviour is related. The first set, the viscosity and the hydrodynamic shell size, have both minimal impact on the $dH/dM_{\max}$, but a smaller magnitude does mean that the FWHM rises slightly. The second set, the anisotropy distribution and the magnetic saturation, behave as opposites. A larger saturation means a smaller FWHM and a larger $dH/dM_{\max}$, which is reversed for the anisotropy. In both graphs is it seen that a change in magnitude changes the middle section of the PRF, while the sides (around $|B_{DC}| > 0.01$ mT) stays mostly the same. Finally, the last parameter: temperature. This seems to have unexpected results, but they suggest that the optimum (a small FWHM and a large $dH/dM_{\max}$) seem to lie around 300 K.

	FWHM			$dH/dM_{\max}$		
	Halved	Normal	Double	Halved	Normal	Double
Temperature	7.09	7.03	16.10	1.00	2.25	1.00
Viscosity	7.29	7.03	6.85	2.31	2.25	2.22
Hydrodynamic shell size	7.44	7.03	6.77	2.34	2.25	2.20
Particle number density	7.03	7.03	7.03	1.12	2.25	4.50
Alternating magnetic field density	6.78	7.03	7.96	1.15	2.25	4.10
Frequency of the magnetic field	7.28	7.03	6.91	1.16	2.25	4.39
Anisotropy distribution	7.92	7.03	13.40	1.90	2.25	0.75
Magnetic saturation	13.54	7.03	3.98	0.58	2.25	8.15
Coil constant	7.03	7.03	7.03	1.12	2.25	4.50

Table 4.1: Predictions of the model, quantified on their PRF as seen in figure 4.1, FWHM in mT and $dH/dM_{\max}$ in mV

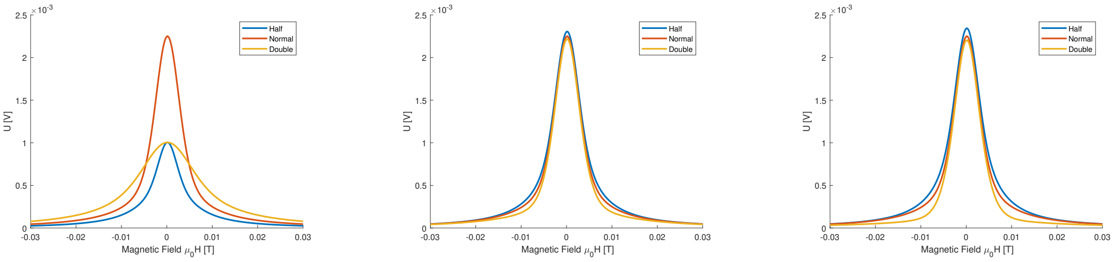

(a) Temperature: halved, normal and doubled

(b) Viscosity: halved, normal and doubled

(c) Hydrodynamic shell size: halved, normal and doubled

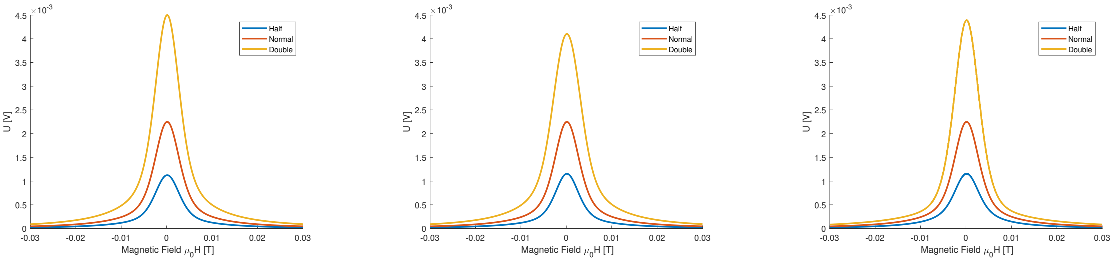

(d) Particle number density: halved, normal and doubled

(e) Alternating magnetic field density: halved, normal and doubled

(f) Frequency of the magnetic field: halved, normal and doubled

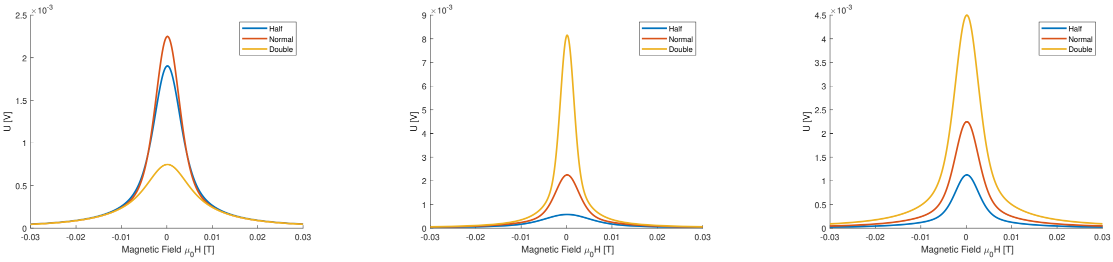

(g) Anisotropy distribution: halved, normal and doubled

(h) Magnetic saturation: halved, normal and doubled

(i) Coil constant: halved, normal and doubled

Figure 4.1: Predictions of the model based on Resovist® in water; normal values: $T = 300$ K, $\eta = 1.0049$ mPa s from [34], $d_c = [5, 21]$ nm, $d_{\text{hdiff}} = 45.2$ nm, $n = 1.5 \cdot 10^{13}$ m^{-3}, $B_{AC} = 0.0014$ T, $f = 2500$ s^{-1}, $K_a = 33.3$ J/m^{3}nm, $K_b = 1000$ J/m^3, $M_s = 300$ kJ/m^{3}T, $\alpha' = 0.1$ from [23] and [35], $S_{coil} = 37.8$ mT/A

The model also has a magnetization curve as output. A magnetization curve of Resovist® in water is seen in figure 4.2, it can be seen that the steepest part of all the shown graphs is on the zero point. Moreover, they quickly flatten out, especially for the Néel en Langevin curve. Finally, it can be seen that the Brownian and Néel parts together form a combined curve, as described in equation 3.8.

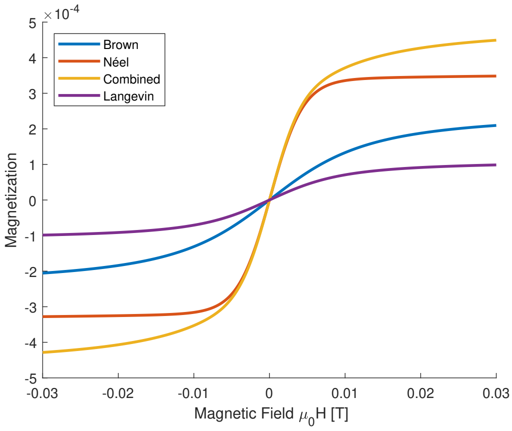

Figure 4.2: Magnetization curve; Resovist® in water

To introduce experimental data, the model was run with a certain parameterset, based upon the available characteristics of Resovist® in water and the measurement conditions of a dataset that was available. This result can be seen in figure 4.3. Here the model had a FWHM of 7.99 mT, the Langevin equation one of 16.19 mT and the actual data set had 8.16 mT. Moreover, the dH/dM_{max} of the model (2.95 mV) corresponds not that well with that of the experimental data (2.31 mV) which can also clearly be seen in the graph. This difference is however not that big as the difference between the Langevin equation and the experimental data. To further enhance the model, it was rewritten such that the model would accept a range of values for the core diameter, as described in chapter 3. As a result, the hydrodynamic diameter and the anisotropy constant differs with a changing core diameter. The core diameter of Resovist® was modelled using two normal distributions added together, which can be seen in figure 4.4. The hydrodynamic diameter was defined as the core diameter plus a constant (d_{hdiff}) and the anisotropy constant trough a linear equation ($K = K_a \cdot d_c + K_b$). These changes resulted in the graphs shown in figure 4.5. It is interesting to note that a smaller bin size (more bins) not always results in a better approximation, the optimum for this case seems to lie with a bin size of 1 nm. As a result, this bin size was also used for the further verification. This, and the fact that the model approaches the experimental data better than the Langevin equation, can be seen in table 4.3.

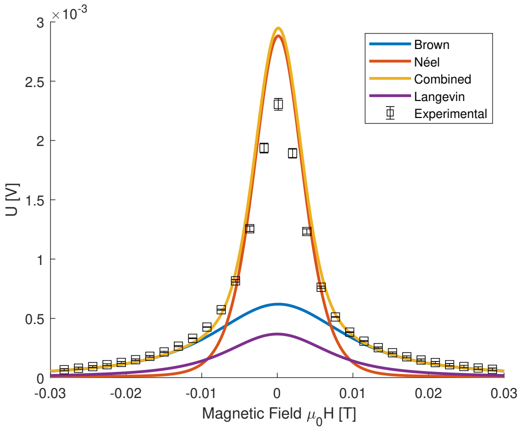

Figure 4.3: PRF of Resovist® in water

Parameter	Quantity
T	300 K
η	1.004 mPa s from [34]
d_c	19 nm
d_{hdiff}	45.2 nm
n	$1.5 \cdot 10^{13}$ m^{-3}
B_{AC}	0.0014 T
f	2500 s^{-1}
K_a	183.3 J/m^{3}nm
K_b	5000 J/m^3
M_s	300 kJ/m^{3}T
α'	0.1 from [23] and [35]
S_{coil}	37.8 mT/A

Table 4.2: Parameters used in Figure 4.3

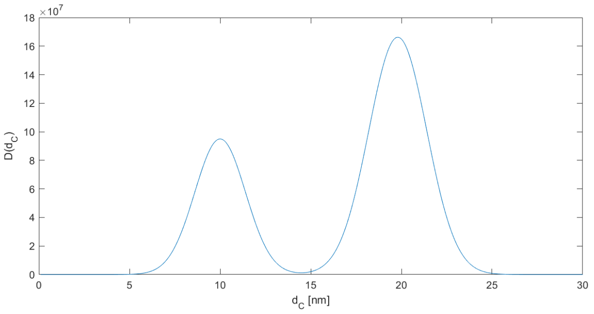

Figure 4.4: Distribution of the Resovist® particle sizes

	Model		Langevin		Data	
	FWHM	dH/dM_{max}	FWHM	dH/dM_{max}	FWHM	dH/dM_{max}
1 bin	7.99	2.95	16.19	0.37	8.16	2.31
5 bins	6.26	2.79	13.03	0.34		
17 bins	7.03	2.25	14.52	0.28		
25 bins	7.12	2.18	14.70	0.27		

Table 4.3: Quantification of the PRF as seen in figure 4.3 and 4.5

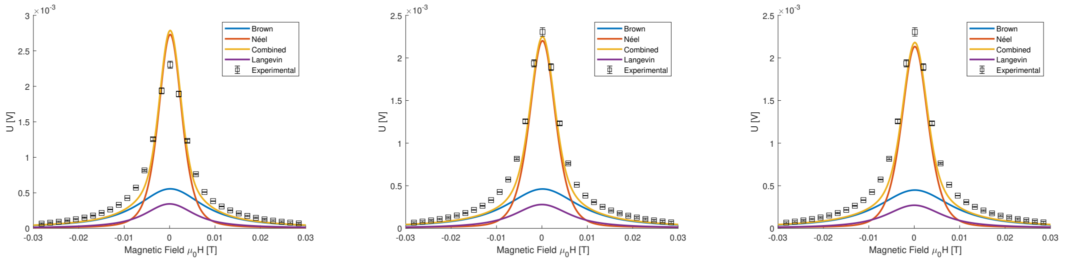

(a) PRF, 5 bins

(b) PRF, 17 bins

(c) PRF, 25 bins

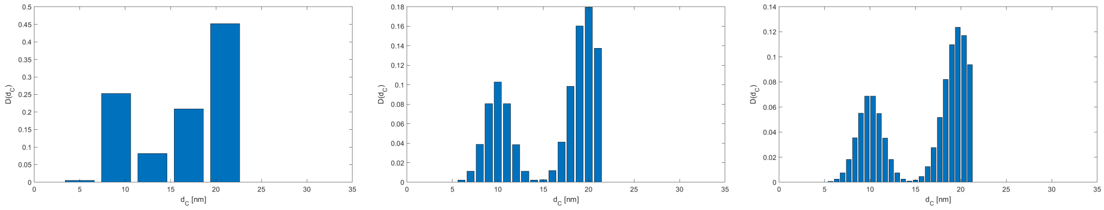

(d) 5 bins of 3.2 nm

(e) 17 bins of 1 nm

(f) 25 bins of 0.64 nm

Figure 4.5: Resovist® in water, various bin sizes; $T = 300$ K, $\eta = 1.0049$ mPa s from [34], $d_c = [5, 21]$ nm, $d_{\text{hdiff}} = 45.2$ nm, $n = 1.5 \cdot 10^{13}$ m^{-3}, $B_{AC} = 0.0014$ T, $f = 2500$ s^{-1}, $K_a = 33.3$ J/m^{3}nm, $K_b = 1000$ J/m^3, $M_s = 300$ kJ/m^{3}T, $\alpha' = 0.1$ from [23] and [35], $S_{coil} = 37.8$ mT/A

4.2 Model verification

4.2.1 Experiment I: Influence of viscosity on performance

To further verify the model, it was run with Resovist® in glycerol instead of water. This fluid has a higher viscosity, which prohibits Brownian relaxation. Because of this it is necessary to use the effective anisotropy constant (K_{eff}) as defined in subsection 2. Apart from the viscosity and this effective anisotropy constant, all values remained the same. The result can be seen in figure 4.6. Again, this PRF was compared to the Langevin equation and to experimental data. The FWHM of the model is 8.41 mT, that of the Langevin equation is 14.52 mT and that of the experimental data is 7.04 mT. Furthermore the dH/dM_{max} is 1.58 mV for the model, 0.28 mV for the Langevin equation and 1.58 mV for the experimental data. This means that the FWHM of the model has a slight difference with the experimental data, which is again better than the Langevin equation.

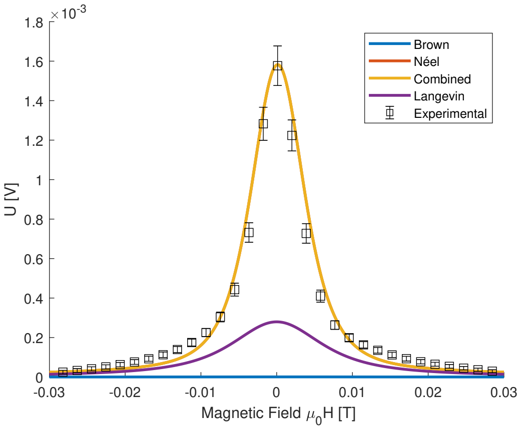

Figure 4.6: PRF of Resovist® in glycerol, where 'Combined' is the result of the Fokker-Plank expansion

Parameter	Quantity
T	300 K
η	0.8 Pa s
d_c	$[5, 21]$ nm
d_{hdiff}	45.2 nm
n	$1.5 \cdot 10^{13}$ m^{-3}
B_{AC}	0.0014 T
f	2500 s^{-1}
K_a	183.3 J/m^{3}nm
K_b	5000 J/m^3
M_s	300 kJ/m^{3}T
α'	0.1 from [23] and [35]
S_{coil}	37.8 mT/A

Table 4.4: Parameters used in Figure 4.6

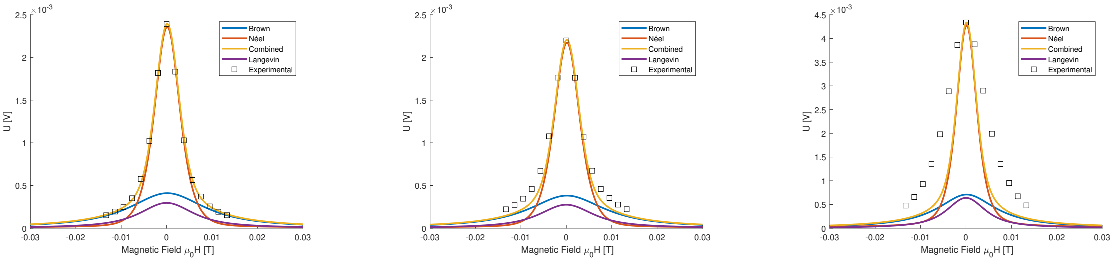

(a) Sienna®; $T = 297$ K, $d_{\text{hdiff}} = 50$ nm, $n = 2.00 \cdot 10^{13}$ m^{-3}, $K_a = 183.3$ J/m^{3}nm, $K_b = 5000$ J/m^3, $M_s = 300$ kJ/m^{3}T

(b) Magtrace®; $T = 296$ K, $d_{\text{hdiff}} = 56.52$ nm, $n = 1.44 \cdot 10^{13}$ m^{-3}, $K_a = 183.3$ J/m^{3}nm, $K_b = 5000$ J/m^3, $M_s = 300$ kJ/m^{3}T

(c) Synomag®; $T = 296$ K, $d_{\text{hdiff}} = 56.52$ nm, $n = 2.21 \cdot 10^{13}$ m^{-3}, $K_a = 75$ J/m^{3}nm, $K_b = 3000$ J/m^3, $M_s = 420$ kJ/m^{3}T

Figure 4.7: PRF of different particles; $\eta = 1.0049$ mPa s from [34], $d_c = [5, 21]$ nm, $B_{AC} = 0.0013$ T, $f = 2500$ s^{-1}, $\alpha' = 0.1$ from [23] and [35], $S_{coil} = 37.8$ mT/A

4.2.2 Experiment II: Influence of iron content on performance

To test the models ability to capture the characteristics of particles other than Resovist®, it was compared with experimental data of Sienna®, Magtrace® and Synomag®, which are -like Resovist®- magnetic tracers. To model these particles like it was done with Resovist® before, n, K_a and K_b were fitted manually since they were not known at the time of writing. This resulted in three PRFs, as seen in figure 4.7. The first thing that stands out is that while Sienna® and Magtrace® are approximated quite well, Synomag® differs plenty. This can also be seen in table 4.5, the FWHM of the model is half the size of that of the experimental data. However, for the two other particles both the FWHM and $dH/dM_{\max}$ are certainly close to the data.

	Sienna®		Magtrace®		Synomag®	
	FWHM	$dH/dM_{\max}$	FWHM	$dH/dM_{\max}$	FWHM	$dH/dM_{\max}$
Model	6.76	2.39	6.84	2.21	5.43	4.34
Langevin	14.28	0.30	14.32	0.28	10.29	0.64
Data	6.68	2.39	7.42	2.21	10.54	4.37

Table 4.5: Different particles quantified on their PRF as seen in figure 4.7, FWHM in mT and $dH/dM_{\max}$ in mV

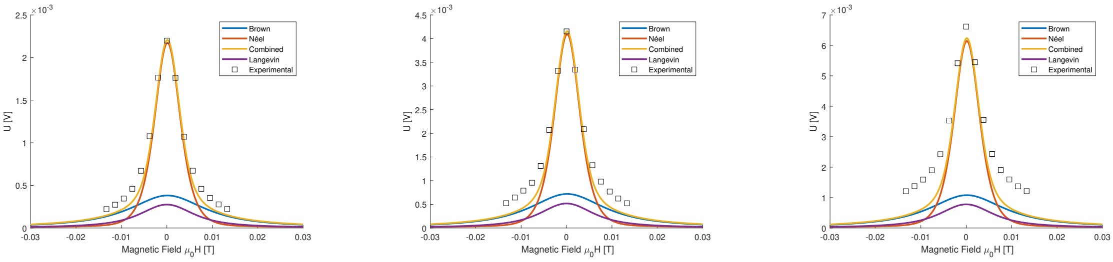

(a) $n = 1.44 \cdot 10^{13}$ m-3 (b) $n = 2.89 \cdot 10^{13}$ m-3 (c) $n = 4.33 \cdot 10^{13}$ m-3

Figure 4.8: PRF of Magtrace®; $T = 296$ K, $d_{\text{hdiff}} = 56.52$ nm, $K_a = 183.3$ J/m^{3}nm, $K_b = 5000$ J/m^3, $M_s = 300$ kJ/m^{3}T, $\eta = 1.0049$ mPa s from [34], $d_c = [5, 21]$ nm, $B_{AC} = 0.0013$ T, $f = 2500$ s^{-1}, $\alpha' = 0.1$ from [23] and [35], $S_{coil} = 37.8$ mT/A

	$n = 1.44 \cdot 10^{13}$ m^{-3}		$n = 2.89 \cdot 10^{13}$ m^{-3}		$n = 4.33 \cdot 10^{13}$ m^{-3}	
	FWHM	dH/dM_{max}	FWHM	dH/dM_{max}	FWHM	dH/dM_{max}
Model	6.84	2.21	6.84	4.16	6.84	6.24
Langevin	14.32	0.28	14.33	0.52	14.32	0.78
Data	7.42	2.21	7.62	4.16	8.20	6.62

Table 4.6: Different densities of Magtrace® quantified on their PRF as seen in figure 4.8, FWHM in mT and dH/dM_{max} in mV

4.2.3 Experiment III: Influence of particle number densities on magnetic performance

Just like in the previous section it is possible to test the model with different datasets to verify it further. Namely, there were datasets available with different particle number densities. The verification was done with Magtrace®. Again, since the number density could not be calculated directly with the available information, the model was fitted with an optimal dH/dM_{max} on the $n = 1.44 \cdot 10^{13}$ m^{-3}. This number density was extended linearly, for instance: if x mg/mL was fitted on y m^{-3}, then $2x$ mg/mL will be $2y$ m^{-3}. The results can be seen in figure 4.8 and the quantification in table 4.6. It is interesting to note that while the FWHM of the model stays constant (the density is a scale factor, this shall be highlighted in the next section) it does slowly change for the experimental data. Moreover, the dH/dM_{max} is optimal for the first two set, while it has a difference of 0.4 mV for the last one, which is also quite small.

Chapter 5

Conclusion

To conclude this attempt at modelling superparamagnetic nanoparticles, one can say that the characteristics of the particles were caught fairly well. The purpose of this research was to capture these particles on their magnetization curves and Particle Response Function (PRF). According to the limited set of data that was used to verify the model, only small differences in the $dH/dM_{\max}$ and in the FWHM are to be expected for predictions made with the model for particles unlike the nanoflower Synomag®. It can be concluded that a bin size of 1 nm gives the best results, while larger and smaller sizes do not reflect the reality well. This could be due to the fact that these particles have certain favorable sizes, possibly not all sizes are even possible. Further research should give more insight.

Finally, while the $dH/dM_{\max}$ was predicted well (since the particle density was fitted) for Synomag® nanoflowers, it was found that the model was not adequate enough in its FWHM. This error might lie with the fact that there is a third relaxation mechanism, which will be spoken about in the Discussion.

Chapter 6

Discussion

To start with, the difference between the model and data for Synomag®. This is, as briefly mentioned before, likely the result of the morphology of the particle. Synomag® consists of flower-like clusters of particles. Due to this clustering, the magnetization of the particles is stronger coupled. The disordered spins within these flowers are suggested to be the reason for a very fast relaxation mechanism, a different mechanism than the Brownian and Néel mechanisms [36]. As a result, the model as it currently stands will not be able to accurately predict such flower-like particles. To solve this issue, more research should be able to find the parameters on which this new mechanism is dependent, and after that, formulate an equation. This will probably be in the form of another Fokker-Planck equation, since both Brownian and Néel are described effectively using such an equation. These equations lend itself well for Legendre expansions, which makes it possible to calculate $\langle x_{New}(t)\rangle$ and $\frac{d}{dt}M_{New}(t)$. This means reformulating equation 3.8:

$$\frac{d}{dt}M(t) = \sqrt{\left(\frac{d}{dt}M_{Brownian}(t)\right)^2 + \left(\frac{d}{dt}M_{N\acute{e}el}(t)\right)^2 + \left(\frac{d}{dt}M_{New}(t)\right)^2} \tag{6.1}$$

In addition, certain values were not always known and were instead fitted on the smallest difference in $dH/dM_{\max}$ between the model output and the data. Temperature, viscosity and such were measured and used as input for the model, but the particle number density (n) and the anisotropy constant distribution (K) were not known. The particle number density can be calculated, if one knows the concentration (c, [g/m^3]) and the molar mass (M, [g/mol]): $n = cN_A/M$. Here N_A is the Avogadro constant ($6.022 \cdot 10^{23}$ mol^{-1}). The anisotropy constant is more complicated. The anisotropy constant increases with the size of the particle [37], which is taken into account in this model using a linear equation. However, this can be enhanced by measuring this constant for multiple bins, with a size of (for instance, as was used in this model) 1 nm. This means separating particles on their core size: (0,1], (1,2], (2,3] nm and so on. This can be done with Asymmetric Flow Field-Flow Fractionation (AF4) [38].

Next, for each bracket one needs to measure the anisotropy constant, by measuring the PRF and fitting the model thereon, since the anisotropy constant is the only unknown value. This constant is sometimes measured by preventing Brownian relaxation (by fixing the particles) and calculating the constant using equation 2.4 [39], which is also a possibility, it could serve as a check. For completeness, it is advised to measure the hydrodynamic shell size for each bracket, as this was assumed to be constant for a changing core size, which might be incorrect. This can be done with dynamic light scattering (DLS) [40]. Knowing this and the anisotropy constant for every core size bracket, one can replace the d_{hdiff} constant and the linear anisotropy equation with the more accurate measured progression.

Furthermore, probably even more important, only for Resovist® the particle size distribution was known, as shown in figure 4.4. Even this distribution might not be accurate. It would be wise to not only measure the hydrodynamic size and anisotropy constant for each core size bracket in the experiment mentioned before, but also the probability. With this in hand, it is possible to calculate the particle size distribution for every kind of particle. This can be done with the AF4 mentioned before, coupled to multiangle light scattering and DLS detectors (AF4-MALS-DLS) as long as the particles are of moderate polydispersity [41].

All changes mentioned in this discussion may reduce the differences between the model and the reality. However, the measurements on particles other than Resovist® were only done once, which means that their precision is not known. But since the measurements on Resovist® were quite precise, it is to be expected that the same will hold for the other particles. Moreover, possibly the accuracy of the measurements could be better, but this is hard to determine. However, it is always good (for precision and accuracy) to repeat the experiments and validate the model further with experimental data from other particles/environments.

The current model has a direct and a indirect clinical significance. The direct significance is the fact that with some (relative) small changes, it could be used to convert a measured voltage from the SPaQ probe into amounts of particles. This means a more direct way of presenting if and in what quantity the particles are accumulated, which could come in handy for finding sentinel nodes and comparing it with different particles/environments. A more indirect significance of this model is that one can use it to create a hypothetical particle, since the model can predict the PRF (for non-flower-like nanoparticles). This hypothetical particle can be tuned to ones preferences on various parameters. Not only enhances this our understanding of these particles but can also help with creating/choosing particles for detection and diagnostics.

Finally, a more technical note which might help future projects save time. The implementation of this model was done in MATLAB® ver. 2020a using ode15. In MATLAB (and most high level programming languages) it is possible to declare global variables, which lends itself perfectly for constants like k_B and γ but (secretly) slows the program down. Avoiding those (feeding every necessary variable to each function), using the Parallel Computing Toolbox (running a parfor with the particle size bins) and other optimizations (such as pre-allocation) means calculating a PRF in 5 minutes instead of in 8 hours. These times were measured on Windows 10 (v2004) with a Intel i5 @ 2.50 GHz.

Samenvatting

In dit onderzoek werd het magnetische gedrag van superparamagnetische nanodeeltjes in verschillende omgevingen gemodelleerd, die hun klinisch nut hebben bij de schlildwachtklierbiopsie. Dit is gedaan door gebruik te maken van de Legendre expansie van twee Fokker-Plank vergelijkingen, een voor Brownian en een voor Néel relaxatie. Met de gecombineerde uitkomst hiervan kan het voltage zoals gemeten wordt met SPaQ benaderd worden. Op basis van verificatie met experimentele data kan gezegd worden dat dit model het gedrag van de geteste deeltjes accuraat weergeeft, met uitzondering van een bloem-vormig deeltje.

References

[1] Giuliano AE, Gangi A. Sentinel Node Biopsy and Improved Patient Care. The Breast Journal. 2015 1;21(1):27–31. Available from: `http://doi.wiley.com/10.1111/tbj.12365`.

[2] Ahmed M, Purushotham AD, Douek M. Novel techniques for sentinel lymph node biopsy in breast cancer: A systematic review. The Lancet Oncology. 2014 7;15(8):e351–e362.

[3] Kolhatkar A, Jamison A, Litvinov D, Willson R, Lee T. Tuning the Magnetic Properties of Nanoparticles. International Journal of Molecular Sciences. 2013 7;14(8):15977–16009. Available from: `http://www.mdpi.com/1422-0067/14/8/15977`.

[4] Pouw JJ. Sentinel lymph node identification with magnetic nanoparticles. University of Twente. Enschede, The Netherlands; 2016. Available from: `http://purl.org/utwente/doi/10.3990/1.9789036540216`.

[5] Van De Loosdrecht MM, Draack S, Waanders S, Schlief JGL, Krooshoop HJG, Viereck T, et al. A novel characterization technique for superparamagnetic iron oxide nanoparticles: The superparamagnetic quantifier, compared with magnetic particle spectroscopy. Review of Scientific Instruments. 2019 2;90(2):024101. Available from: `http://aip.scitation.org/doi/10.1063/1.5039150`.

[6] Mok CW, Tan SM, Zheng Q, Shi L. Network meta-analysis of novel and conventional sentinel lymph node biopsy techniques in breast cancer. BJS Open. 2019 3;3(4):bjs5.50157. Available from: `https://onlinelibrary.wiley.com/doi/abs/10.1002/bjs5.50157`.

[7] Thill M, Kurylcio A, Welter R, van Haasteren V, Grosse B, Berclaz G, et al. The Central-European SentiMag study: Sentinel lymph node biopsy with superparamagnetic iron oxide (SPIO) vs. radioisotope. Breast. 2014;23(2):175–179. Available from: `https://pubmed.ncbi.nlm.nih.gov/24484967/`.

[8] Büscher K, Helm CA, Gross C, Glöckl G, Romanus E, Weitschies W. Nanoparticle Composition of a Ferrofluid and Its Effects on the Magnetic Properties. Langmuir. 2004 3;20(6):2435–2444. Available from: `https://pubs.acs.org/doi/full/10.1021/la030261x`.

[9] Osuna J, De Caro D, Amiens C, Chaudret B, Snoeck E, Respaud M, et al. Synthesis, characterization, and magnetic properties of cobalt nanoparticles from an organometallic precursor. The Journal of Physical Chemistry®. 1996;100(35):14571–14574. Available from: `https://pubs.acs.org/doi/full/10.1021/jp961086e`.

[10] Schlief JGL. Searching for the cause of the SuperParamagnetic Quantifier measurement drift. University of Twente; 2020.

[11] Poole CP, Barikhtar VGVG. Encyclopedic dictionary of condensed matter physics. Volume 1, A-M. Elsevier; 2004.

[12] Bakenecker A, Ahlborg M, Debbeler C, Kaethner C, Lüdtke-Buzug K. Magnetic Particle Imaging. In: Precision Medicine: Tools and Quantitative Approaches. Elsevier Inc.; 2018. p. 183–228.

[13] Boča R. Chapter 7 Types of magnetic materials. In: Current Methods in Inorganic Chemistry. vol. 1. Elsevier; 1999. p. 345–370.

[14] Pankhurst QA, Connolly J, Jones SK, Dobson J. Applications of magnetic nanoparticles in biomedicine. Journal of Physics D: Applied Physics. 2003;36(13):R167–R181. Available from: `http://dx.doi.org/10.1088/0022-3727/36/13/201`.

[15] Visscher M, Waanders S, Krooshoop HJG, Ten Haken B. Selective detection of magnetic nanoparticles in biomedical applications using differential magnetometry. Journal of Magnetism and Magnetic Materials. 2014 9;365:31–39.

[16] Reeves DB, Weaver JB. Approaches for modeling magnetic nanoparticle dynamics. Critical Reviews in Biomedical Engineering. 2014;42(1):85–93.

[17] Coffey WT, Kalmykov YP. The Langevin Equation. vol. 27 of World Scientific Series in Contemporary Chemical Physics. WORLD SCIENTIFIC; 2012. Available from: `https://www.worldscientific.com/worldscibooks/10.1142/8195`.

[18] López-Ruiz R, Luis F, González V, Millán A, García-Palacios JL. Nonlinear response of single-molecule nanomagnets: Equilibrium and dynamical. Physical Review B - Condensed Matter and Materials Physics. 2005 12;72(22):224433.

[19] Deatsch AE, Evans BA. Heating efficiency in magnetic nanoparticle hyperthermia. Journal of Magnetism and Magnetic Materials. 2014 3;354:163–172.

[20] Odenbach S. Colloidal magnetic fluids : basics, development and application of ferrofluids. Springer Verlag; 2009.

[21] Krishnan KM. Fundamentals and applications of magnetic materials. 3rd ed. Oxford: Oxford University Press; 2017.

[22] Coffey WT, Cregg PJ, Kalmykov YUP. On the Theory of Debye and Néel Relaxation of Single Domain Ferromagnetic Particles. In: Advances in Chemical Physics. Advances in Chemical Physics. John Wiley & Sons; 1992. p. 263–464. Available from: `https://doi.org/10.1002/9780470141410.ch5`.

[23] Deissler RJ, Wu Y, Martens MA. Dependence of Brownian and Néel relaxation times on magnetic field strength. Medical Physics. 2013 12;41(1):012301. Available from: `http://doi.wiley.com/10.1118/1.4837216`.

[24] Ludwig F, Eberbeck D, Löwa N, Steinhoff U, Wawrzik T, Schilling M, et al. Characterization of magnetic nanoparticle systems with respect to their magnetic particle imaging performance. Biomedizinische Technik. 2013 12;58(6):535–545.

[25] Kötitz R, Weitschies W, Trahms L, Semmler W. Investigation of Brownian and Néel relaxation in magnetic fluids. Journal of Magnetism and Magnetic Materials. 1999 7;201(1-3):102–104.

[26] Parker FT, Foster MW, Margulies DT, Berkowitz AE. Spin canting, surface magnetization, and finite-size effects in γ-Fe2O3 particles. Physical Review B. 1993;47(13):7885–7891.

[27] Respaud M. Magnetization process of noninteracting ferromagnetic cobalt nanoparticles in the superparamagnetic regime: Deviation from Langevin law. Journal of Applied Physics. 1999 7;86(1):556–561. Available from: `http://aip.scitation.org/doi/10.1063/1.370765`.

[28] Chantrell RW, Walmsley N, Gore J, Maylin M. Calculations of the susceptibility of interacting superparamagnetic particles. Physical Review B - Condensed Matter and Materials Physics. 2001 12;63(2):024410.

[29] Chen DX, Sanchez A, Taboada E, Roig A, Sun N, Gu HC. Size determination of superparamagnetic nanoparticles from magnetization curve. Journal of Applied Physics. 2009 4;105(8):083924. Available from: `http://aip.scitation.org/doi/10.1063/1.3117512`.

[30] Zheng B, Lu K, Konkle JJ, Hensley DW, Keselman P, Orendorff RD, et al. Magnetic particle imaging. In: Design and Applications of Nanoparticles in Biomedical Imaging. Springer International Publishing; 2016. p. 69–93. Available from: `https://link.springer.com/chapter/10.1007/978-3-319-42169-8_4`.

[31] Pablico-Lansigan MH, Situ SF, Samia ACS. Magnetic particle imaging: Advancements and perspectives for real-time in vivo monitoring and image-guided therapy. Nanoscale. 2013 5;5(10):4040–4055.

[32] Eyck Q. Ex-vivo sentinel lymph node mapping in colorectal carcinoma using superparamagnetic iron-oxide nanoparticles: a pilot study. University Twente; 2019.

[33] Atlas SW. Magnetic Resonance Imaging of the Brain and Spine, 4th ed., Vol. 1 and 2. American Journal of Neuroradiology. 2009 5;30(5):e76–e77.

[34] Martens MA, Deissler RJ, Wu Y, Bauer L, Yao Z, Brown R, et al. Modeling the Brownian relaxation of nanoparticle ferrofluids: Comparison with experiment. Medical Physics. 2013 1;40(2):022303. Available from: `http://doi.wiley.com/10.1118/1.4773869`.

[35] Weizenecker J, Gleich B, Rahmer J, Borgert J. Micro-magnetic simulation study on the magnetic particle imaging performance of anisotropic mono-domain particles. Physics in Medicine and Biology. 2012;57(22):7317–7327. Available from: `http://dx.doi.org/10.1088/0031-9155/57/22/7317`.

[36] Bender P, Fock J, Frandsen C, Hansen MF, Balceris C, Ludwig F, et al. Relating Magnetic Properties and High Hyperthermia Performance of Iron Oxide Nanoflowers. Journal of Physical Chemistry C. 2018 2;122(5):3068–3077.

[37] Löwa N, Knappe P, Wiekhorst F, Eberbeck D, Thunemann AF, Trahms L. How Hydrodynamic Fractionation Influences MPI Performance of Resovist. IEEE Transactions on Magnetics. 2015 2;51(2).

[38] Gilliland D. Asymmetric Flow Field Flow Fractionation (AF4) and Inductively Coupled Plasma-Mass Spectrometry (ICP-MS) methods as a means to determine nanoparticle number size distributions of silver nanoparticle dispersions Report of stage 1 of inter-laboratory trial. EU publications. 2017. Available from: `https://ec.europa.eu/jrc`.

[39] Yoon S. Determination of the Temperature Dependence of the Magnetic Anisotropy Constant in Magnetite Nanoparticles. Journal of the Korean Physical Society. 2011 11;59(5):3069–3073.

[40] Fissan H, Ristig S, Kaminski H, Asbach C, Epple M. Comparison of different characterization methods for nanoparticle dispersions before and after aerosolization. Analytical Methods. 2014 9;6(18):7324–7334.

[41] Caputo F, Arnould A, Bacia M, Ling WL, Rustique E, Texier I, et al. Measuring Particle Size Distribution by Asymmetric Flow Field Flow Fractionation: A Powerful Method for the Preclinical Characterization of Lipid-Based Nanoparticles. Molecular Pharmaceutics. 2019 2;16(2):756–767.